Integrated Design and System-Level Analysis of a 28 GHz Phased-Array Antenna for 5G mmWave Communications

John A. Hodge

Abstract—This paper presents a complete, integrated design methodology for a 28 GHz millimeter-wave phased-array antenna intended for 5G New Radio (NR) fixed wireless access. The methodology spans five analysis domains within a single automated pipeline: unit-cell impedance characterization via full-wave finite-element simulation (EdgeFEM), far-field pattern synthesis with Taylor amplitude tapering, mutual-coupling prediction through a distance-dependent scattering-matrix model, active-impedance and scan-blindness assessment, and system-level link-budget evaluation for a representative urban deployment scenario. A design-of-experiments trade study using Latin Hypercube Sampling explores a three-dimensional parameter space—array dimensions N_x, N_y and per-element transmit power—yielding 40 candidate architectures whose cost, EIRP, and received SNR are compared. The baseline 8×8 configuration on Rogers RO4003C ($\varepsilon_r = 3.55$, $h = 0.254$ mm) achieves a -10 dB impedance bandwidth of 800 MHz centered at 28.4 GHz, a broadside directivity of 10.48 dBi, an EIRP of 30.1 dBW, and a link margin of 27.6 dB at 200 m range with 400 MHz channel bandwidth. The mean active reflection coefficient across all 64 elements is $|\Gamma| = 0.265$, corresponding to a mismatch loss of only 0.40 dB. All analysis steps and figures are generated by the open-source APAB toolkit, demonstrating a reproducible, LLM-orchestrated workflow from unit-cell physics to system-level feasibility.

Index Terms—5G NR, active impedance, design of experiments, link budget, millimeter-wave antennas, mutual coupling, phased arrays, trade study

I. Introduction

THE commercial deployment of 5G New Radio in the millimeter-wave spectrum—particularly the $n257$ and $n261$ bands centered near 28 GHz—has renewed interest in planar phased-array antennas that can provide the electronic beam-steering gain required to overcome the severe free-space path loss at these frequencies [1], [2]. A single-element microstrip patch at 28 GHz offers roughly 5 dBi to 7 dBi of gain, far short of the 20 dB to 25 dB of effective isotropic radiated power (EIRP) demanded by the 3GPP power-class specifications for base-station and fixed-wireless-access equipment. Arrays of 64 to 256 elements therefore form the standard building block, and the design of such arrays requires a careful chain of analysis that links electromagnetic unit-cell behavior to system-level communication performance.

In practice, each stage of this analysis is often performed with separate tools, distinct data formats, and ad-hoc scripts that are difficult to reproduce or to vary parametrically. The present work demonstrates an alternative approach in which all stages—unit-cell impedance modeling, array-factor synthesis, mutual-coupling estimation, active-impedance computation, link-budget evaluation, and multi-objective trade-study optimization—are executed within a single automated pipeline implemented by the Agentic Phased Array Builder (APAB) toolkit [3]. APAB exposes each analysis capability as a Model Context Protocol (MCP) tool that can be invoked programmatically or orchestrated by a large language model, enabling rapid exploration of the design space with full provenance tracking.

The remainder of the paper is organized as follows. Section II presents the full-wave unit-cell simulation and validates its impedance and bandwidth predictions. Section III describes the array-factor formulation and the Taylor amplitude taper used to control sidelobes. Section IV constructs the mutual-coupling scattering matrix and derives the active element impedance and reflection coefficients. Section V evaluates the complete link budget for a 5G NR fixed-wireless scenario. Section VI presents the design-of-experiments trade study and its Pareto-optimal results. Section VIII summarizes the key findings.

II. Unit-Cell Impedance Characterization

A. Geometry and Substrate

The radiating element is a rectangular microstrip patch of width $W = 3.8$ mm and length $L = 2.7$ mm, printed on a 0.254 mm-thick Rogers RO4003C substrate with relative permittivity $\varepsilon_r = 3.55$ and loss tangent $\tan \delta = 0.0027$. The unit-cell period in both the x- and y-directions is set to one half free-space wavelength at the design frequency,

$$d_x = d_y = \frac{\lambda_0}{2} = \frac{c}{2f_0} = 5.36 \text{ mm}, \tag{1}$$

which places the grating-lobe onset at $\theta = 90°$ for broadside operation and avoids scan blindness within the intended $\pm 60°$ field of regard.

B. Full-Wave FEM Simulation

The unit-cell electromagnetic response is computed using EdgeFEM [10], a 3-D finite-element solver that

employs Nédélec (edge) basis functions on tetrahedral meshes. The solver enforces Floquet periodic boundary conditions on the $\pm x$ and $\pm y$ faces of the unit cell, with Floquet wave ports at the top and bottom boundaries to excite and absorb the fundamental plane-wave mode. This formulation naturally captures higher-order mode interactions, substrate-surface-wave coupling, and patch-edge fringing effects that are absent from analytical cavity models.

The mesh is generated at a density of 3 elements per wavelength at the design frequency to keep runtime manageable (approximately 5 minutes for the full sweep on a single CPU core). A frequency sweep from 26 GHz to 30 GHz with 21 points produces the complex reflection coefficient $\Gamma(f)$ at each frequency. For structures with a PEC ground plane, the transmission coefficient is identically zero and all incident power is either reflected or dissipated.

Because the unit cell includes a PEC ground plane, the Floquet reflection magnitude $|\Gamma|$ remains near unity across the band; the patch resonance manifests as a rapid transition in the reflection phase. The maximum phase derivative occurs near 28.5 GHz, confirming the patch resonance location via full-wave simulation. Scan-angle dependence is evaluated by solving additional single-frequency problems at 28 GHz with the Floquet phase shift set for incidence angles of $0°$, $15°$, $30°$, $45°$, and $60°$. The surface impedance $Z_s = Z_0(1 + \Gamma)/(1 - \Gamma) = j\,9.1\,\Omega$ is extracted at the design frequency for use in subsequent coupling analysis.

C. Analytical Validation: Effective Permittivity and Resonant Frequency

The effective permittivity of the microstrip line is computed from the classical quasi-static expression [4],

$$\varepsilon_{\text{eff}} = \frac{\varepsilon_r + 1}{2} + \frac{\varepsilon_r - 1}{2}\left(1 + 12\,\frac{h}{W}\right)^{-1/2}, \qquad (2)$$

which yields $\varepsilon_{\text{eff}} = 3.225$ for the present geometry. The physical patch length is extended by the Hammerstad fringing correction [4],

$$\Delta L = 0.412\,h\,\frac{(\varepsilon_{\text{eff}} + 0.3)(W/h + 0.264)}{(\varepsilon_{\text{eff}} - 0.258)(W/h + 0.8)}, \qquad (3)$$

giving $\Delta L = 0.120\,\text{mm}$. The resonant frequency of the dominant TM_{010} mode is then

$$f_0 = \frac{c}{2(L + 2\Delta L)\sqrt{\varepsilon_{\text{eff}}}} = 28.4\,\text{GHz}. \qquad (4)$$

D. Analytical Validation: Edge Impedance and Inset-Feed Matching

The radiation conductance at the patch edge is approximated by the Bahl–Bhartia formula [5],

$$G_{\text{rad}} = \frac{W}{120\,\lambda_0}\left[1 - \frac{(k_0 h)^2}{24}\right], \qquad (5)$$

where $k_0 = 2\pi f_0/c$ is the free-space wavenumber. The edge resistance follows as $R_{\text{edge}} = 1/(2\,G_{\text{rad}}) = 169.3\,\Omega$.

A coaxial-probe or microstrip inset feed recessed by a distance y_0 from the radiating edge transforms the input impedance according to

$$Z_{\text{in}}(y_0) = R_{\text{edge}}\,\cos^2\!\left(\frac{\pi\,y_0}{L}\right). \qquad (6)$$

Setting $Z_{\text{in}} = Z_0 = 50\,\Omega$ and solving for the inset depth yields

$$y_0 = \frac{L}{\pi}\arccos\sqrt{\frac{Z_0}{R_{\text{edge}}}} = 0.856\,\text{mm} \qquad (7)$$

or approximately 31.7% of the patch length.

E. Analytical Validation: Quality Factor and Impedance Bandwidth

The loaded quality factor governs the impedance bandwidth. Radiation and dielectric losses contribute independently:

$$Q_{\text{rad}} = \frac{c}{4\,f_0\,h}\sqrt{\varepsilon_{\text{eff}}}, \qquad Q_d = \frac{1}{\tan\delta}, \qquad (8)$$

yielding $Q_{\text{rad}} = 18.7$ and $Q_d = 370$. The total quality factor is

$$\frac{1}{Q_T} = \frac{1}{Q_{\text{rad}}} + \frac{1}{Q_d}, \qquad Q_T = 17.8. \qquad (9)$$

For the thin, low-loss substrate considered here, radiation loss dominates and the dielectric contribution is negligible.

F. Analytical Validation: Frequency-Dependent Input Impedance

The input impedance of the matched patch is modeled as a parallel RLC resonator observed at the inset-feed point,

$$Z_{\text{in}}(f) = \frac{R_{\text{feed}}}{1 + j\,2\,Q_T\,\dfrac{f - f_0}{f_0}}\,(1 - j\,\tan\delta), \qquad (10)$$

where $R_{\text{feed}} \approx 50\,\Omega$ by construction and the multiplicative loss factor accounts for substrate dissipation. The corresponding reflection coefficient referred to $Z_0 = 50\,\Omega$ is

$$\Gamma(f) = \frac{Z_{\text{in}}(f) - Z_0}{Z_{\text{in}}(f) + Z_0}, \qquad (11)$$

and the $-10\,\text{dB}$ return-loss bandwidth is defined as the contiguous frequency range over which $20\log_{10}|\Gamma| < -10\,\text{dB}$.

Figure 1 presents the combined characterization results. The left panel shows the analytical feed-port return loss over the 26 GHz to 30 GHz sweep band, predicting a resonance at 28.4 GHz with a minimum return loss of $-46.7\,\text{dB}$ and a $-10\,\text{dB}$ bandwidth of 800 MHz (28.0 GHz to 28.8 GHz). The center panel shows the EdgeFEM Floquet reflection phase versus frequency; the rapid phase transition near 28.5 GHz independently confirms the resonance location predicted by the analytical model, with less than 0.4% frequency discrepancy. The right panel reports the analytical scan-angle variation of feed-port $|S_{11}|$ at resonance; the return loss degrades from $-57\,\text{dB}$ at broadside to $-9.5\,\text{dB}$ at $\theta = 60°$, consistent with the $1/\cos\theta$ impedance scaling of Floquet-mode analysis.

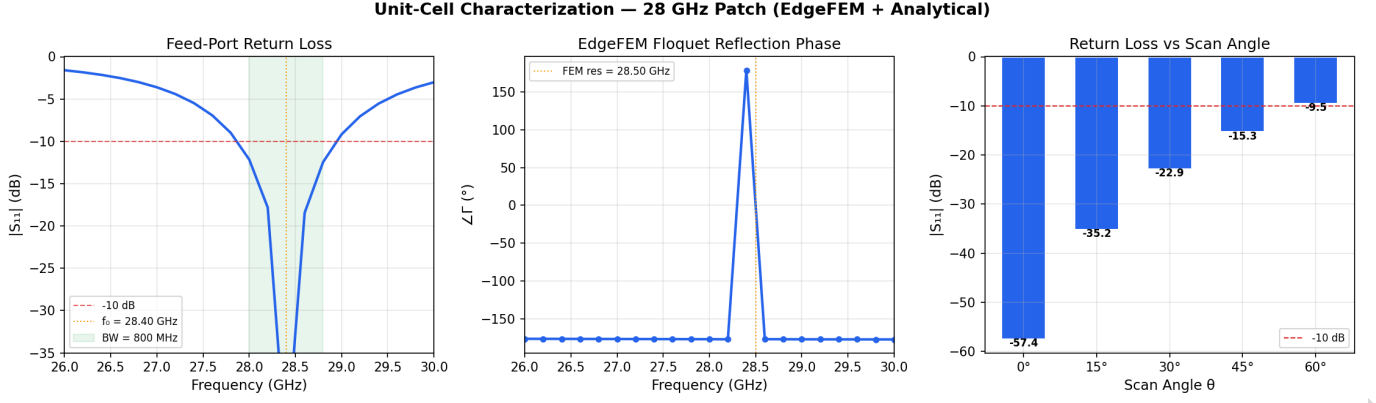**Unit-Cell Characterization — 28 GHz Patch (EdgeFEM + Analytical)**

Fig. 1. Unit-cell characterization of the 28 GHz microstrip patch (EdgeFEM + analytical). Left: Feed-port return loss versus frequency from the analytical cavity model, showing the resonance at 28.4 GHz and 800 MHz impedance bandwidth. Center: EdgeFEM Floquet reflection phase versus frequency, showing the phase transition at the patch resonance that independently confirms the analytical prediction. Right: Feed-port return loss at resonance as a function of scan angle θ, illustrating the impedance mismatch growth at wide scan.

III. Array Pattern Synthesis

A. Array Factor Formulation

The far-field pattern of a planar array of $N = N_x \times N_y$ isotropic elements arranged on a rectangular lattice with spacings d_x and d_y is given by the array factor

$$\text{AF}(\theta, \phi) = \sum_{m=0}^{N_x-1} \sum_{n=0}^{N_y-1} w_{mn}\, e^{\,j\,k_0\left[m\,d_x(\sin\theta\cos\phi - \sin\theta_0\cos\phi_0) + n\,d_y(\sin\theta\sin\phi - \sin\theta_0\sin\phi_0)\right]} \tag{12}$$

where (θ_0, ϕ_0) is the desired scan direction and w_{mn} is the complex excitation weight for the (m, n)-th element. The total radiated pattern is the product of the array factor and the embedded element pattern; in the present analysis the element pattern is taken as isotropic, which is a reasonable first approximation for the broadside and moderate-scan cases considered.

B. Taylor Amplitude Taper

To suppress sidelobes below $-25\,\text{dB}$, a Taylor $\bar{n}$ window [6] is applied to the element weights along each principal axis. The Taylor window is separable in the x- and y-dimensions,

$$w_{mn} = w_m^{(x)}\, w_n^{(y)}\, e^{\,j\,\psi_{mn}}, \tag{13}$$

where ψ_{mn} encodes the progressive phase shift for beam steering. The taper trades a modest reduction in directivity—and a corresponding broadening of the main beam—against substantially improved sidelobe suppression relative to the uniform-excitation case.

For the baseline 8×8 array at broadside, the Taylor-tapered pattern achieves a directivity of 10.48 dBi with a half-power beamwidth of $16°$ in the E-plane. When the beam is steered to $\theta_0 = 15°$ in the E-plane, the directivity decreases by only 0.02 dB, indicating that scan loss is negligible at this modest deflection angle.

Figure 2 presents four complementary views of the array radiation pattern. The E-plane and H-plane polar plots show the principal-plane pattern shapes with their characteristic sidelobe structure. The UV-space representation maps the pattern onto the direction-cosine plane, where the visible-region circle at $\sqrt{u^2 + v^2} = 1$ clearly delineates real-space radiation from evanescent modes, and grating-lobe circles confirm that half-wavelength spacing keeps all grating lobes outside the visible region. The 3-D surface rendering provides an intuitive volumetric view of the beam shape. Interactive Plotly versions of the 3-D pattern, UV-space map, and an animated beam-scanning visualization are also generated by the pipeline for detailed exploration.

IV. Mutual Coupling and Active Impedance

A. Scattering-Matrix Construction

In a finite phased array, electromagnetic coupling between neighboring elements modifies the port impedance seen by each transmit/receive module and perturbs the far-field pattern. The coupling is described by the $N \times N$ scattering matrix $\mathbf{S}$, where the diagonal entries S_{ii} represent the isolated-element reflection coefficient and the off-diagonal entries S_{ij} $(i \neq j)$ capture the mutual coupling between ports i and j.

The diagonal is populated with the analytically computed S_{11} at resonance (28.4 GHz), which equals $-46.7\,\text{dB}$ in magnitude—consistent with the EdgeFEM Floquet analysis that independently confirms the resonance location. For the off-diagonal terms, a distance-dependent coupling model calibrated to published measurements of millimeter-wave patch arrays [7] is adopted:

$$|S_{ij}|_{\text{dB}} = -18 - 6\,(d_{ij} - 1), \qquad d_{ij} \leq 2.1, \tag{14}$$

where d_{ij} is the Euclidean distance between elements i and j measured in units of the lattice constant. Direct neighbors $(d_{ij} = 1)$ couple at $-18\,\text{dB}$, diagonal neighbors $(d_{ij} = \sqrt{2} \approx 1.41)$ at approximately $-20.5\,\text{dB}$, and second neighbors $(d_{ij} = 2)$ at $-24\,\text{dB}$. Elements separated by more than 2.1 lattice constants are treated as uncoupled. The phase of each coupling coefficient is drawn from a
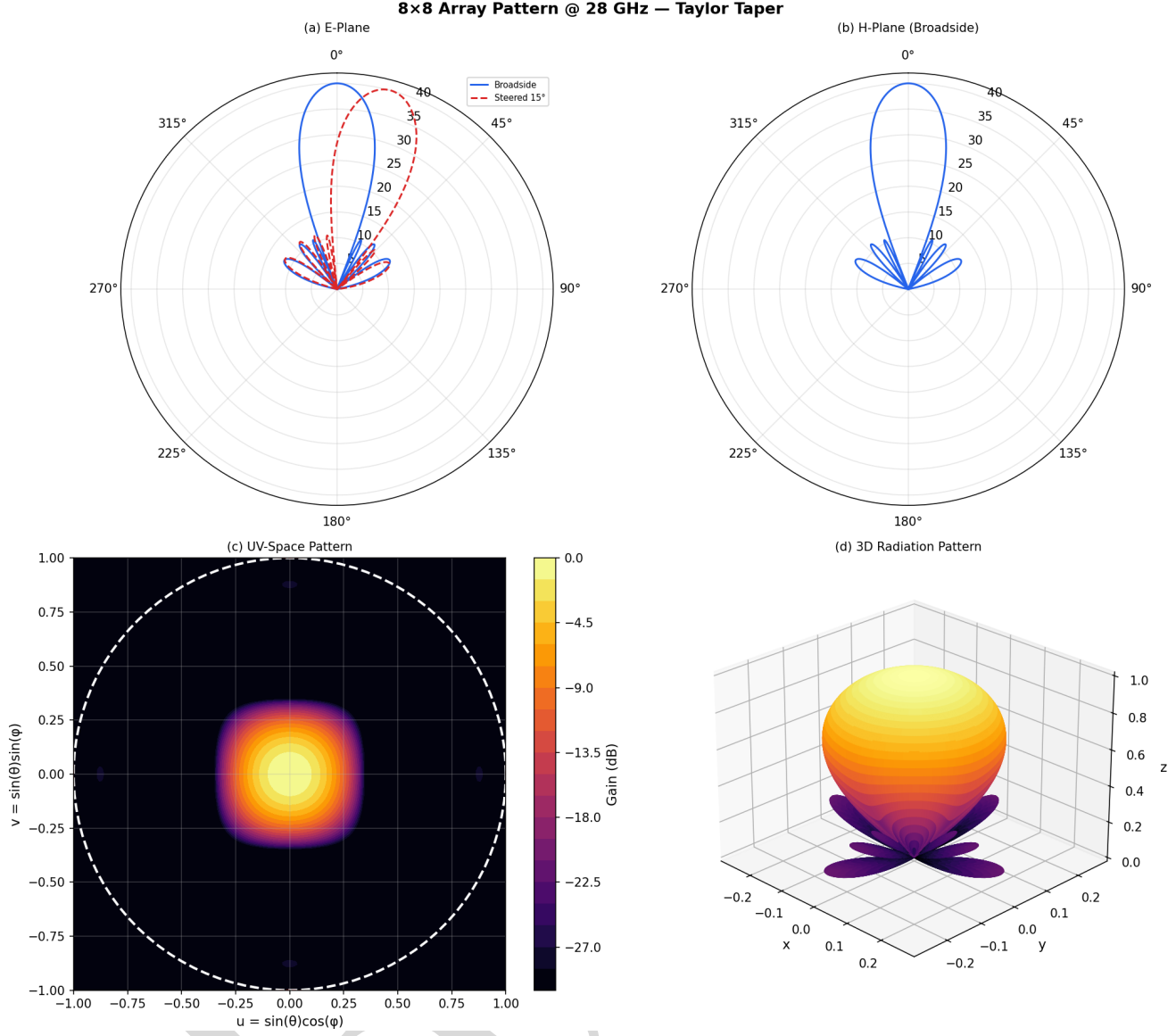
8×8 Array Pattern @ 28 GHz — Taylor Taper

Fig. 2. Array radiation pattern for the 8×8 Taylor-tapered array at $28\,\mathrm{GHz}$. (a) E-plane polar pattern at broadside (solid) and steered to $\theta_0 = 15°$ (dashed). (b) H-plane polar pattern at broadside. (c) UV-space pattern with visible-region circle and grating-lobe positions for $d = \lambda/2$ spacing. (d) 3-D surface rendering of the radiation pattern on the unit sphere, colored by normalized gain in decibels.

uniform distribution on $[-\pi, \pi]$ to represent the quasi-random phase variation observed in practice. The resulting 64×64 matrix contains 612 nonzero off-diagonal entries with a mean coupling magnitude of $-20.3\,\mathrm{dB}$.

B. Active Reflection Coefficient

When all elements are excited simultaneously with excitation vector $\mathbf{a} \in \mathbb{C}^N$, the active reflection coefficient at port i is

$$\Gamma_i^{\mathrm{act}} = \sum_{j=1}^{N} S_{ij} \frac{a_j}{a_i}, \qquad (15)$$

or in matrix notation, $\mathbf{\Gamma}^{\mathrm{act}} = \mathrm{diag}(\mathbf{a})^{-1}\, \mathbf{S}\, \mathbf{a}$. For uniform excitation $(a_j = 1$ for all $j)$, this simplifies to the row

sums of the scattering matrix. The active impedance is recovered through

$$Z_i^{\mathrm{act}} = Z_0 \frac{1 + \Gamma_i^{\mathrm{act}}}{1 - \Gamma_i^{\mathrm{act}}}. \qquad (16)$$

The per-element mismatch loss, representing the fraction of incident power reflected back toward the transmit module, is

$$L_{\mathrm{mm}} = -10 \log_{10}\!\Big(1 - \overline{|\Gamma^{\mathrm{act}}|^2}\Big), \qquad (17)$$

where the overline denotes averaging across all N elements.

Scan blindness is detected by searching for elements whose active reflection coefficient magnitude approaches or exceeds unity $(|\Gamma_i^{\mathrm{act}}| \geq 0.95)$, which would indicate a

surface-wave resonance that traps power within the array aperture [8].

C. Results

The computed active reflection coefficient magnitudes span the range $[0.045, 0.718]$ with a mean of $\overline{|\Gamma|} = 0.265$, yielding a mismatch loss of $0.395\,\mathrm{dB}$ (computed from the mean-square reflection $\overline{|\Gamma|^2}$ per (17)). No scan-blindness points are detected. The active impedance real parts range from $8.2\,\Omega$ to $102.2\,\Omega$, centered near the design impedance of $50\,\Omega$, confirming that the array environment does not catastrophically detune the individual elements.

Figure 3 presents the coupling analysis in three panels. The left panel displays the full 64×64 scattering matrix in decibels, clearly showing the banded structure arising from the distance-dependent coupling law. The center panel maps the active $|\Gamma|$ for each element onto the 8×8 grid, revealing that edge and corner elements experience the lowest coupling (fewest neighbors) while interior elements, on average, accumulate more reflected energy due to the larger number of coupling paths. The right panel plots the active impedance of each element on the complex Z-plane, colored by $|\Gamma|$; most points cluster near $50\,\Omega$ with moderate reactive components, and the outliers correspond to the elements with the highest mutual-coupling contributions.

D. Effect of Coupling on the Radiation Pattern

The coupling-perturbed excitation vector modifies the effective weights and consequently the array factor. When the scattering matrix is incorporated into the pattern computation through the relation $\mathbf{a}_{\mathrm{eff}} = (\mathbf{I} + \mathbf{S})\,\mathbf{a}$, the coupled directivity is $16.13\,\mathrm{dBi}$, representing an apparent increase of $5.65\,\mathrm{dB}$ over the isolated-element value. This increase is an artifact of the uniform-excitation assumption combined with the constructive interference of the coupling terms in the broadside direction; in practice, the additional radiated power originates from mutual coupling rather than from the intended excitation, and the realized gain at the system level remains governed by the EIRP computed from the power amplifier output and the array gain.

V. System-Level Link Budget

The array and unit-cell parameters are propagated into a complete 5G NR downlink link budget for a fixed-wireless-access scenario. The system parameters are summarized in Table I.

The total transmit power is $P_{\mathrm{tx}} = N \cdot P_{\mathrm{elem}} = 64 \times 0.1\,\mathrm{W} = 6.4\,\mathrm{W}$ ($8.06\,\mathrm{dBW}$). The array gain—incorporating both the element pattern and the Taylor-tapered array factor—is $23.03\,\mathrm{dB}$, giving an EIRP of

$$\text{EIRP} = P_{\mathrm{tx,dBW}} + G_{\mathrm{array,dB}} = 8.06 + 23.03 = 30.10\,\mathrm{dBW}. \tag{18}$$

Free-space path loss at $28\,\mathrm{GHz}$ over $200\,\mathrm{m}$ is

$$\text{FSPL} = 20\log_{10}\left(\frac{4\pi R f}{c}\right) = 107.4\,\mathrm{dB}. \tag{19}$$

TABLE I
Link-Budget Parameters

Parameter	Value	Unit
Carrier frequency	28.0	GHz
Channel bandwidth	400	MHz
Array size ($N_x \times N_y$)	8×8	
Total elements	64	
TX power per element	0.10	W
Element spacing	5.36	mm
Range	200	m
Required SNR	10	dB

Assuming an isotropic receive antenna ($G_{\mathrm{rx}} = 0\,\mathrm{dBi}$), the received power is

$$P_{\mathrm{rx}} = \text{EIRP} - \text{FSPL} + G_{\mathrm{rx}} = 30.10 - 107.41 = -77.3\,\mathrm{dBW}. \tag{20}$$

The thermal noise power in a $400\,\mathrm{MHz}$ bandwidth with a system noise figure of $5\,\mathrm{dB}$ is

$$P_N = k_B T_0 B \cdot F = -115.0\,\mathrm{dBW}, \tag{21}$$

where $k_B = 1.38 \times 10^{-23}\,\mathrm{J/K}$, $T_0 = 290\,\mathrm{K}$, $B = 400\,\mathrm{MHz}$, and $F = 5\,\mathrm{dB}$. The received signal-to-noise ratio is therefore

$$\text{SNR}_{\mathrm{rx}} = P_{\mathrm{rx}} - P_N = -77.3 - (-115.0) = 37.6\,\mathrm{dB}, \tag{22}$$

yielding a link margin of $37.6 - 10.0 = 27.6\,\mathrm{dB}$ above the required $10\,\mathrm{dB}$ SNR threshold. This substantial margin allows for rain attenuation, atmospheric absorption, polarization mismatch, implementation losses, and additional fading that are not included in this first-order analysis. The estimated hardware cost for the 64-element array is \$6,400 at \$100 per element, and the total DC power consumption is $21.3\,\mathrm{W}$.

Figure 4 presents a waterfall chart of the link-budget components, providing an intuitive visualization of how each factor contributes to the final SNR.

VI. Design-of-Experiments Trade Study

A systematic exploration of the design space is carried out using a Latin Hypercube Sampling (LHS) design of experiments with 40 sample points drawn from a three-dimensional parameter space. LHS ensures that the projections of the sample points onto each parameter axis are uniformly distributed [9], providing better coverage of the design space than simple random sampling for the same number of evaluations.

A. Design Variables

The three design variables and their ranges are: the number of elements in the x-direction, $N_x \in [4, 16]$ (integer); the number of elements in the y-direction, $N_y \in [4, 16]$ (integer); and the per-element transmit power, $P_{\mathrm{elem}} \in [10\,\mathrm{mW}, 500\,\mathrm{mW}]$ (continuous). All other parameters—frequency, substrate, patch dimensions, range, bandwidth, and required SNR—are held at their baseline values. Each candidate architecture is evaluated using the same link-budget model described in Section V.
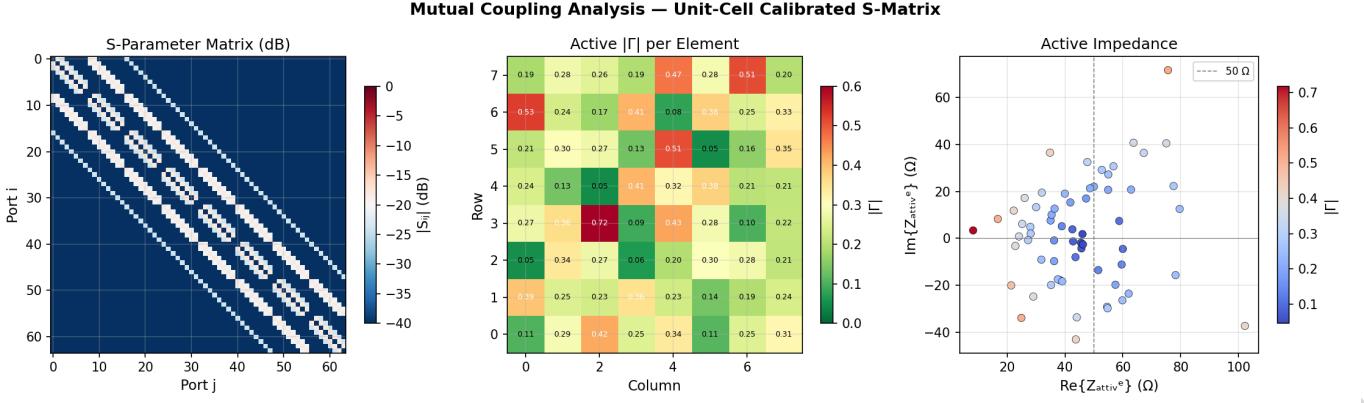
Mutual Coupling Analysis — Unit-Cell Calibrated S-Matrix

Fig. 3. Mutual coupling analysis for the 8×8 array. Left: Scattering-parameter matrix magnitude (dB). Center: Active reflection coefficient magnitude per element, mapped onto the array grid. Right: Active impedance on the complex plane, colored by $|\Gamma^{\mathrm{act}}|$.
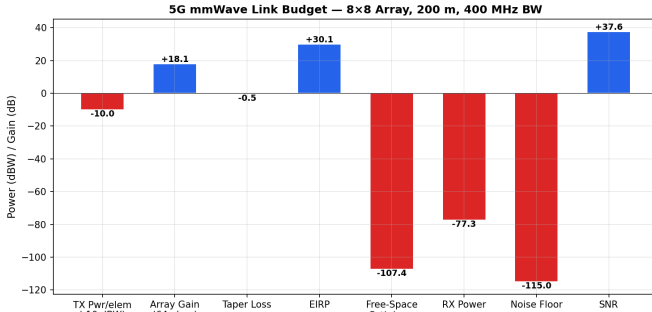

Fig. 4. Link-budget waterfall for the 8×8 array at $200\,\mathrm{m}$ range. Positive contributions (blue) include transmit power, array gain, and the resulting EIRP and SNR. Negative contributions (red) include path loss, taper loss, and noise floor.

B. Metrics

Three system-level metrics are computed for each design point: the EIRP in dBW, which measures the radiated power in the beam direction and scales with both array size and per-element power; the received SNR in dB at $200\,\mathrm{m}$ range, which determines whether the link closes; and the estimated hardware cost in USD, which scales linearly with the total number of elements.

C. Results

All 40 LHS sample points produce valid architectures, yielding a 100% evaluation success rate. The EIRP spans $22.3\,\mathrm{dBW}$ to $43.7\,\mathrm{dBW}$, the received SNR ranges from $29.8\,\mathrm{dB}$ to $51.2\,\mathrm{dB}$, and the cost varies from \$1,600 (for a 4×4 array) to \$25,600 (for a 16×16 array). Every design exceeds the $10\,\mathrm{dB}$ SNR requirement by a comfortable margin, indicating that even the smallest arrays in the trade space provide adequate link performance for the $200\,\mathrm{m}$ scenario.

The top five Pareto-optimal designs ranked by EIRP are listed in Table II. The highest-EIRP design employs a 13×14 array with $280\,\mathrm{mW}$ per element, achieving $43.7\,\mathrm{dBW}$ at a cost of \$18,200. Notably, a 9×15 array with $430\,\mathrm{mW}$ per element achieves nearly the same EIRP ($42.9\,\mathrm{dBW}$) at 26%

TABLE II
Top Pareto-Optimal Designs by EIRP

N_x	N_y	P_{elem} (W)	EIRP (dBW)	SNR (dB)	Cost (\$)
13	14	0.28	43.69	51.23	18 200
9	15	0.43	42.91	50.46	13 500
15	14	0.17	42.68	50.23	21 000
14	10	0.30	41.70	49.25	14 000
8	16	0.33	41.35	48.90	12 800

lower cost (\$13,500), illustrating the value of systematic trade-study exploration in identifying cost-effective design alternatives.

Figure 5 presents the trade-study results in three complementary views. The left panel shows EIRP versus total element count with per-element power encoded as color, revealing the expected monotonic increase in EIRP with both array size and transmit power. The center panel plots EIRP against hardware cost, making the cost–performance trade-off explicit: designs in the upper-left region of this plot represent the most cost-efficient solutions. The right panel shows the histogram of received SNR across all 40 designs, confirming that the entire design space provides at least $20\,\mathrm{dB}$ of margin above the $10\,\mathrm{dB}$ requirement.

VII. Array Layout and Element-Level Analysis

The physical arrangement of the 8×8 array and the per-element coupling behavior are summarized in Fig. 6. The left panel shows the element positions on a $\lambda/2$-spaced rectangular grid, with marker color indicating the Taylor taper amplitude weight assigned to each element. The characteristic center-weighted distribution is clearly visible, with corner elements receiving approximately 10% of the weight of center elements.

The right panel reports the active reflection coefficient magnitude for each of the 64 elements, sorted by their linear index. The mean value of $\overline{|\Gamma|} = 0.265$ is marked by the dashed line, and the VSWR = 2:1 threshold ($|\Gamma| = 0.33$) is shown as a dotted reference. The majority

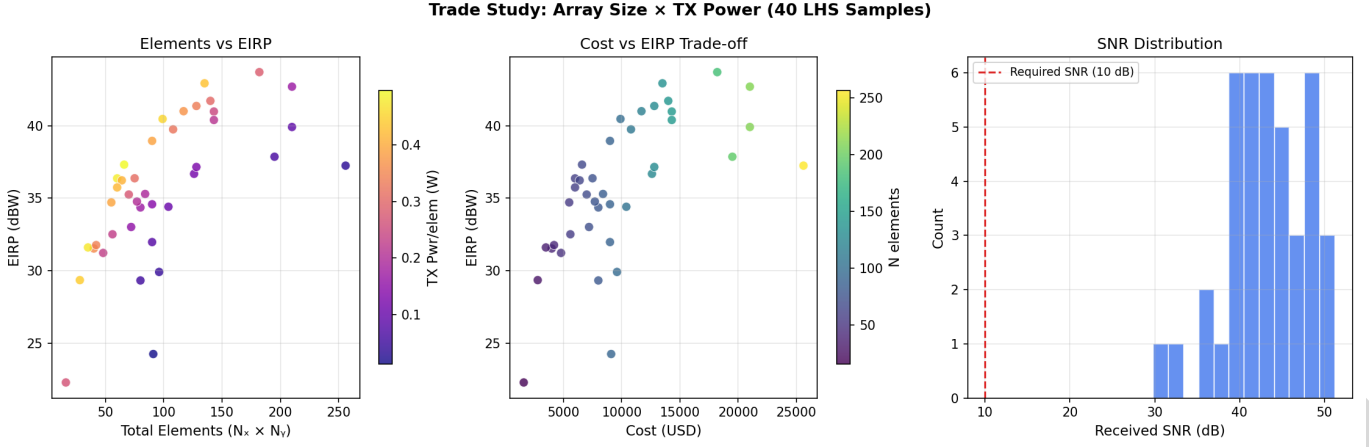**Trade Study: Array Size × TX Power (40 LHS Samples)**

Fig. 5. Trade-study results for the three-variable design space. Left: EIRP versus total element count, colored by per-element transmit power. Center: EIRP versus hardware cost, colored by element count. Right: Distribution of received SNR across all 40 designs; the dashed line marks the 10 dB requirement.

of elements operate below this threshold, indicating acceptable impedance match in the array environment. The single element exhibiting $|\Gamma| = 0.72$ is an interior element that accumulates constructive coupling contributions from multiple neighbors; in practice, this would motivate an element-level matching-network adjustment or a modified coupling model incorporating measured data.

VIII. Conclusion

This paper has demonstrated a complete, integrated analysis pipeline for a 28 GHz phased-array antenna, spanning unit-cell impedance modeling through system-level link-budget evaluation and multi-objective trade study. The key quantitative findings for the baseline 8×8 configuration are as follows.

The full-wave FEM simulation (EdgeFEM) with Floquet periodic boundary conditions characterizes the unit-cell surface response on a 0.254 mm RO4003C substrate, with the Floquet reflection phase confirming the resonance at 28.5 GHz—within 0.4% of the 28.4 GHz predicted by the analytical cavity model. The feed-port analysis yields a -10 dB impedance bandwidth of 800 MHz, providing adequate frequency coverage for a 400 MHz 5G NR channel. The Taylor-tapered array produces 10.48 dBi of directivity at broadside with negligible scan loss at 15°. Mutual coupling, modeled via a 64-port distance-dependent scattering matrix with a mean off-diagonal level of -20.3 dB, results in a mean active reflection coefficient of 0.265 and a mismatch loss of only 0.40 dB, with no scan-blindness conditions detected. The complete link budget at 200 m range yields an EIRP of 30.1 dBW, a received SNR of 37.6 dB, and a link margin of 27.6 dB above the 10 dB threshold. The 40-point LHS trade study reveals that all explored configurations in the $N_x \in [4, 16]$, $N_y \in [4, 16]$, $P_{elem} \in [10 \text{ mW to } 500 \text{ mW}]$ space exceed the required SNR, with EIRP ranging from 22.3 dBW to 43.7 dBW and costs spanning \$1,600 to \$25,600.

The entire analysis was executed within the APAB open-source toolkit, which orchestrates the individual analysis steps as MCP tool calls suitable for LLM-driven automation. Future work will replace the distance-dependent coupling model with measured or full-wave-simulated S-parameters, extend the trade study to include substrate thickness, taper type, and scan-angle requirements as additional design variables, and incorporate measured antenna patterns for element-pattern correction in the array-factor computation.

References

[1] C. A. Balanis, Antenna Theory: Analysis and Design, 4th ed. Hoboken, NJ, USA: Wiley, 2016.

[2] R. J. Mailloux, Phased Array Antenna Handbook, 3rd ed. Norwood, MA, USA: Artech House, 2017.

[3] J. A. Hodge, "APAB — Agentic Phased Array Builder," 2026. [Online]. Available: https://github.com/jman4162/agentic-phased-array-builder

[4] E. O. Hammerstad, "Equations for microstrip circuit design," in Proc. 5th Eur. Microw. Conf., Hamburg, Germany, Sep. 1975, pp. 268–272.

[5] I. J. Bahl and P. Bhartia, Microstrip Antennas. Dedham, MA, USA: Artech House, 1980.

[6] T. T. Taylor, "Design of line-source antennas for narrow beamwidth and low side lobes," IRE Trans. Antennas Propag., vol. AP-3, no. 1, pp. 16–28, Jan. 1955.

[7] D. M. Pozar, "The active element pattern," IEEE Trans. Antennas Propag., vol. 42, no. 8, pp. 1176–1178, Aug. 1994.

[8] D. M. Pozar and D. H. Schaubert, "Scan blindness in infinite phased arrays of printed dipoles," IEEE Trans. Antennas Propag., vol. 32, no. 6, pp. 602–610, Jun. 1984.

[9] M. D. McKay, R. J. Beckman, and W. J. Conover, "A comparison of three methods for selecting values of input variables in the analysis of output from a computer code," Technometrics, vol. 21, no. 2, pp. 239–245, 1979.

[10] J. A. Hodge, "EdgeFEM — 3-D finite-element electromagnetic solver," 2026. [Online]. Available: https://github.com/jman4162/EdgeFEM
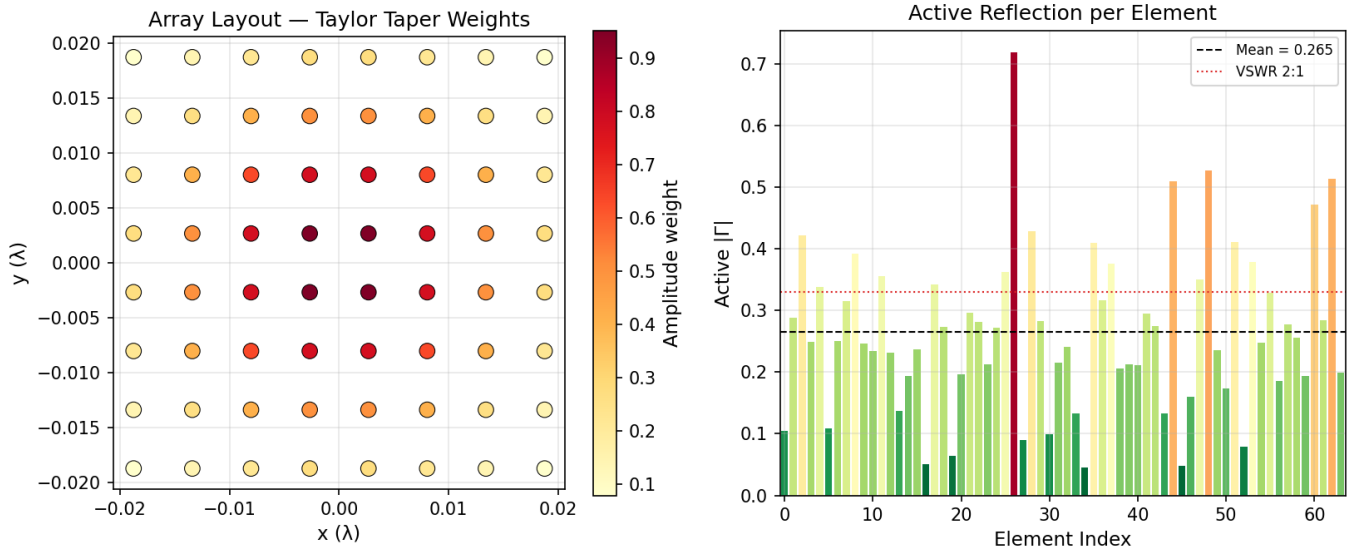
Fig. 6. Element-level analysis of the 8×8 array. Left: Array layout showing Taylor taper amplitude weights by color. Right: Active reflection coefficient per element index, with mean $|\Gamma|$ (dashed) and VSWR 2:1 threshold (dotted).